



**HAL**  
open science

## High abundance ratio of $^{13}\text{CO}$ to $\text{C}^{18}\text{O}$ toward photon-dominated regions in the Orion-A giant molecular cloud

Yoshito Shimajiri, Yoshimi Kitamura, Masao Saito, Munetake Momose, Fumitaka Nakamura, Kazuhito Dobashi, Tomomi Shimoikura, Hiroyuki Nishitani, Akifumi Yamabi, Chihomi Hara, et al.

### ► To cite this version:

Yoshito Shimajiri, Yoshimi Kitamura, Masao Saito, Munetake Momose, Fumitaka Nakamura, et al.. High abundance ratio of  $^{13}\text{CO}$  to  $\text{C}^{18}\text{O}$  toward photon-dominated regions in the Orion-A giant molecular cloud. *Astronomy and Astrophysics - A&A*, 2014, 564, pp.A68. 10.1051/0004-6361/201322912 . cea-01236279

**HAL Id: cea-01236279**

**<https://cea.hal.science/cea-01236279>**

Submitted on 1 Dec 2015

**HAL** is a multi-disciplinary open access archive for the deposit and dissemination of scientific research documents, whether they are published or not. The documents may come from teaching and research institutions in France or abroad, or from public or private research centers.

L'archive ouverte pluridisciplinaire **HAL**, est destinée au dépôt et à la diffusion de documents scientifiques de niveau recherche, publiés ou non, émanant des établissements d'enseignement et de recherche français ou étrangers, des laboratoires publics ou privés.

# High abundance ratio of $^{13}\text{CO}$ to $\text{C}^{18}\text{O}$ toward photon-dominated regions in the Orion-A giant molecular cloud<sup>\*</sup>

Yoshito Shimajiri<sup>1,2,3</sup>, Yoshimi Kitamura<sup>4</sup>, Masao Saito<sup>2,5</sup>, Munetake Momose<sup>6</sup>, Fumitaka Nakamura<sup>2</sup>, Kazuhito Dobashi<sup>7</sup>, Tomomi Shimoikura<sup>7</sup>, Hiroyuki Nishitani<sup>2,3</sup>, Akifumi Yamabi<sup>7</sup>, Chihomi Hara<sup>2,8</sup>, Sho Katakura<sup>7</sup>, Takashi Tsukagoshi<sup>6</sup>, Tomohiro Tanaka<sup>9</sup>, and Ryohei Kawabe<sup>2,5</sup>

<sup>1</sup> Laboratoire AIM, CEA/DSM-CNRS-Université Paris Diderot, IRFU/Service d'Astrophysique, CEA Saclay, 91191 Gif-sur-Yvette, France

e-mail: Yoshito.Shimajiri@cea.fr

<sup>2</sup> National Astronomical Observatory of Japan, 2-21-1 Osawa, Mitaka, 181-8588 Tokyo, Japan

<sup>3</sup> Nobeyama Radio Observatory, 462-2 Nobeyama, Minamimaki, Minamisaku, 384-1305 Nagano, Japan

<sup>4</sup> Institute of Space and Astronautical Science, Japan Aerospace Exploration Agency, 3-1-1 Yoshinodai, Chuo-ku, 252-5210 Sagami-hara, Japan

<sup>5</sup> Joint ALMA Observatory, Alonso de Cordova 3107 Vitacura, 763 0355 Santiago, Chile

<sup>6</sup> Institute of Astrophysics and Planetary Sciences, Ibaraki University, 2-1-1 Bunkyo, Mito, 310-8512 Ibaraki, Japan

<sup>7</sup> Department of Astronomy and Earth Sciences, Tokyo Gakugei University, Koganei, 184-8501 Tokyo, Japan

<sup>8</sup> The University of Tokyo, 7-3-1 Hongo Bunkyo, 113-0033 Tokyo, Japan

<sup>9</sup> Department of Physical Science, Osaka Prefecture University, Gakuen 1-1, Sakai, 599-8531 Osaka, Japan

Received 25 October 2013 / Accepted 24 February 2014

## ABSTRACT

**Aims.** We derive physical properties such as the optical depths and the column densities of  $^{13}\text{CO}$  and  $\text{C}^{18}\text{O}$  to investigate the relationship between the far ultraviolet (FUV) radiation and the abundance ratios between  $^{13}\text{CO}$  and  $\text{C}^{18}\text{O}$ .

**Methods.** We have carried out wide-field ( $0.4 \text{ deg}^2$ ) observations with an angular resolution of  $25.8''$  ( $\sim 0.05 \text{ pc}$ ) in  $^{13}\text{CO}$  ( $J = 1-0$ ) and  $\text{C}^{18}\text{O}$  ( $J = 1-0$ ) toward the Orion-A giant molecular cloud using the Nobeyama 45 m telescope in the on-the-fly mode.

**Results.** Overall distributions and velocity structures of the  $^{13}\text{CO}$  and  $\text{C}^{18}\text{O}$  emissions are similar to those of the  $^{12}\text{CO}$  ( $J = 1-0$ ) emission. The optical depths of the  $^{13}\text{CO}$  and  $\text{C}^{18}\text{O}$  emission lines are estimated to be  $0.05 < \tau_{^{13}\text{CO}} < 1.54$  and  $0.01 < \tau_{\text{C}^{18}\text{O}} < 0.18$ , respectively. The column densities of the  $^{13}\text{CO}$  and  $\text{C}^{18}\text{O}$  emission lines are estimated to be  $0.2 \times 10^{16} < N_{^{13}\text{CO}} < 3.7 \times 10^{17} \text{ cm}^{-2}$  and  $0.4 \times 10^{15} < N_{\text{C}^{18}\text{O}} < 3.5 \times 10^{16} \text{ cm}^{-2}$ , respectively. The abundance ratios between  $^{13}\text{CO}$  and  $\text{C}^{18}\text{O}$ ,  $X_{^{13}\text{CO}}/X_{\text{C}^{18}\text{O}}$ , are found to be 5.7–33.0. The mean value of  $X_{^{13}\text{CO}}/X_{\text{C}^{18}\text{O}}$  in the nearly edge-on photon-dominated regions is found to be  $16.47 \pm 0.10$ , which is a third larger than that the solar system value of 5.5. The mean value of  $X_{^{13}\text{CO}}/X_{\text{C}^{18}\text{O}}$  in the other regions is found to be  $12.29 \pm 0.02$ . The difference of the abundance ratio is most likely due to the selective FUV photodissociation of  $\text{C}^{18}\text{O}$ .

**Key words.** ISM: abundances – ISM: clouds – photon-dominated region – ISM: individual objects: Orion-A

## 1. Introduction

Far ultraviolet (FUV:  $6 \text{ eV} < h\nu < 13.6 \text{ eV}$ ) radiation emitted from massive stars influences the structure, chemistry, thermal balance, and evolution of the neutral interstellar medium of galaxies (Hollenbach & Tielens 1997). Furthermore, stars are formed in the interstellar medium (ISM) irradiated by the FUV radiation. Hence, studies of the influence of FUV are crucial for understanding the process of star formation. Regions where FUV photons dominate the energy balance or chemistry of the gas are called photon-dominated regions (PDRs). The FUV emission selectively dissociates CO isotopes more effectively than CO because of the difference in the self-shielding (Glassgold et al. 1985; Yurimoto & Kuramoto 2004; Liszt 2007; Röllig & Ossenkopf 2013). The FUV intensity at the

wavelengths of the dissociation lines for abundant CO decays rapidly on the surface of molecular clouds since the FUV emission becomes optically very thick at these wavelengths. For less abundant  $\text{C}^{18}\text{O}$ , which has shifted absorption lines owing to the difference in the vibrational-rotational energy levels, the decay of FUV is much lower. As a result,  $\text{C}^{18}\text{O}$  molecules are expected to be selectively dissociated by UV photons, even in a deep molecular cloud interior. In the dark cloud near a young cluster (IC 5146, for example), the ratio of the  $^{13}\text{CO}$  to  $\text{C}^{18}\text{O}$  fractional abundance,  $X_{^{13}\text{CO}}/X_{\text{C}^{18}\text{O}}$ , considerably exceeds the solar system value of 5.5 at visual extinction ( $A_V$ ) values of less than 10 mag (Fig. 19 in Lada et al. 1994). This trend indicates the selective UV photodissociation of  $\text{C}^{18}\text{O}$ . A variation of the abundance ratios of the isotopes is also reported (Wilson 1999; Wang et al. 2009). For example, the values of  $X_{^{13}\text{CO}}/X_{\text{C}^{18}\text{O}}$  in the solar system, local ISM, Galactic center, and Large Magellanic Cloud (LMC) are measured to be 5.5, 6.1, 12.5, and 40.8. In the Milky way, the isotopic ratio is proportional to the distance from our Galactic center (Wilson 1999).

\* The data and the FITS files of Figs. 1, 2a,b, and 3a are only available at the CDS via anonymous ftp to [cdsarc.u-strasbg.fr](http://cdsarc.u-strasbg.fr) (130.79.128.5) or via <http://cdsarc.u-strasbg.fr/viz-bin/qcat?J/A+A/564/A68>

The Orion-A giant molecular cloud (Orion-A GMC) is the nearest GMC ( $d = 400$  pc; Menten et al. 2007; Sandstrom et al. 2007; Hirota et al. 2008) and is one of the best studied star-forming regions (e.g., Bally et al. 1987; Dutrey et al. 1993; Tatematsu et al. 1999; Johnstone & Bally 1999; Shimajiri et al. 2008, 2009; Takahashi et al. 2008; Davis et al. 2009; Berné et al. 2010; Takahashi et al. 2013; Lee et al. 2013). In the northern part of the Orion-A GMC, there are three HII regions, M 42, M 43, and NGC 1977 (Goudis 1982). From the comparison of the AzTEC 1.1 mm and the Nobeyama 45 m  $^{12}\text{CO}$  ( $J = 1-0$ ), and Midcourse Space Experiment (MSX)  $8\ \mu\text{m}$  emissions (from polycyclic aromatic hydrocarbons, PAHs) maps, Shimajiri et al. (2011) have identified seven PDRs and their candidates in the northern part of the Orion-A GMC: 1) Orion Bar; 2) the M43 Shell; 3) a dark lane south filament (DLSF); 4–7) the four regions A–D. Since the stratification among these distributions can be recognized, the PDR candidates are likely to be influenced by the FUV emission from the Trapezium star cluster and from NU Ori in nearly edge-on configuration. Thus, the Orion-A GMC is one of the most suitable targets for investigating the PDRs. Recently, Shimajiri et al. (2013) carried out wide-field ( $0.17\ \text{deg}^2$ ) and high-angular resolution ( $21.3'' \sim 0.04$  pc) observations in [CI] line toward the Orion-A GMC. The mapping region includes the nearly edge-on PDRs and the four PDR candidates of the Orion Bar, DLSF, M43 Shell, and Region D. The overall distribution of the [CI] emission coincides with that of the  $^{12}\text{CO}$  emission in the nearly edge-on PDRs, which is inconsistent with the prediction by the plane-parallel PDR model (Hollenbach & Tielens 1999). The [CI] distribution in the Orion-A GMC is found to be more similar to those of the  $^{13}\text{CO}$  ( $J = 1-0$ ),  $\text{C}^{18}\text{O}$  ( $J = 1-0$ ), and  $\text{H}^{13}\text{CO}^+$  ( $J = 1-0$ ) lines rather than that of the  $^{12}\text{CO}$  ( $J = 1-0$ ) line in the inner part of the cloud, suggesting that the [CI] emission is not limited to the cloud surface, but is tracing the dense, inner parts of the cloud.

This paper is organized as follows: in Sect. 2, the Nobeyama 45 m observations are described. In Sect. 3, we present the  $^{13}\text{CO}$  and  $\text{C}^{18}\text{O}$  maps of the Orion-A GMC and estimate the optical depths of the  $^{13}\text{CO}$  and  $\text{C}^{18}\text{O}$  gas and the column densities of these molecules. In Sect. 4, we discuss the variation of the ratio of the  $^{13}\text{CO}$  to  $\text{C}^{18}\text{O}$  fractional abundance in terms of the FUV radiation. In Sect. 5, we summarize our results. Detailed distributions of the filaments and dense cores and their velocity structure and mass will be reported in a forthcoming paper.

## 2. NRO 45 m observations and data reduction

In 2010 and 2013, we carried out  $^{13}\text{CO}$  ( $J = 1-0$ ) and  $\text{C}^{18}\text{O}$  ( $J = 1-0$ ) mapping observations toward a  $0.4\ \text{deg}^2$  region in the northern part of the Orion-A GMC with the 25-element focal plane receiver BEARS installed in the 45 m telescope at the Nobeyama Radio Observatory (NRO). The  $^{13}\text{CO}$  ( $J = 1-0$ ) and  $\text{C}^{18}\text{O}$  ( $J = 1-0$ ) data were obtained separately. Figure 1 shows the  $^{13}\text{CO}$  and  $\text{C}^{18}\text{O}$  observing areas. At 110 GHz, the telescope has a beam size of  $16''$  (HPBW) and a main beam efficiency,  $\eta_{\text{MB}}$ , of 38% in the 2010 season and 36% in 2013, which are from observatory measurements at 110 GHz using the S100 receiver. The beam separation of the BEARS is  $41':1$  on the sky plane (Sunada et al. 2000). As the back end, we used 25 sets of 1024 channel auto-correlators (ACs) which have a 32 MHz bandwidth and a frequency resolution of 37.8 kHz (Sorai et al. 2000). The frequency resolution corresponds to a velocity resolution of  $\sim 0.1\ \text{km s}^{-1}$  at 110 GHz. During the

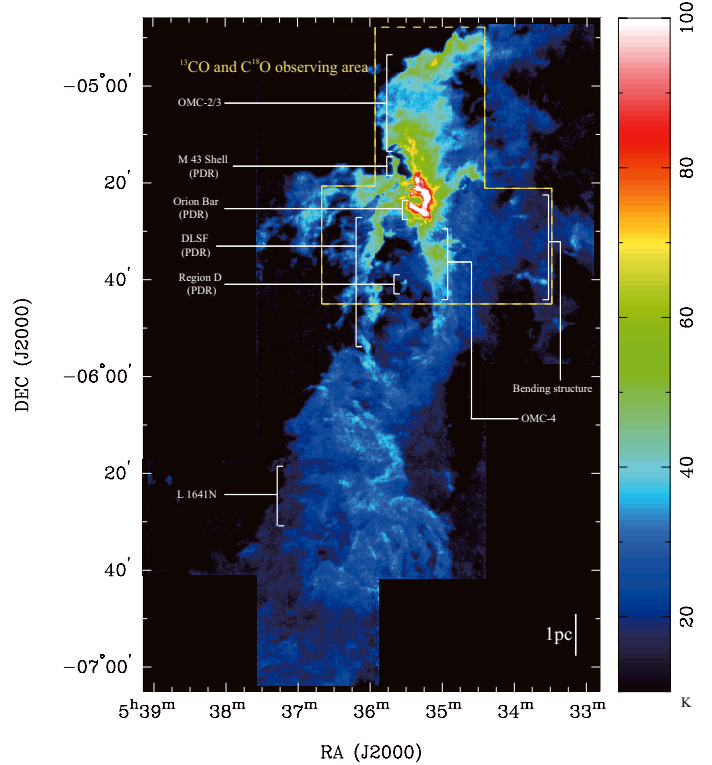


**Fig. 1.** Peak intensity map in the  $^{12}\text{CO}$  ( $J = 1-0$ ) line in units of K ( $T_{\text{MB}}$ ). The data are from Shimajiri et al. (2011) and Nakamura et al. (2012). A dashed box shows the  $^{13}\text{CO}$  ( $J = 1-0$ ) and  $\text{C}^{18}\text{O}$  ( $J = 1-0$ ) observing region. The  $^{12}\text{CO}$  data in FITS format are available at the NRO web page via <http://www.nro.nao.ac.jp/~nro45mrt/html/results/data.html> and at the CDS.

observations, the system noise temperatures were in a range from 270 K to 470 K in the double sideband (DSB). The standard chopper wheel method was used to convert the observed signal to the antenna temperature,  $T_{\text{A}}$ , in units of K, corrected for the atmospheric attenuation. The data are given in terms of the main-beam brightness temperature,  $T_{\text{MB}} = T_{\text{A}}^*/\eta_{\text{MB}}$ . The telescope pointing was checked every 1.5 h by observing the SiO maser source Ori KL, and was better than  $3''$  throughout the entire observation. The intensity scales of the BEARS 25 beams are different from each other owing to the varying sideband ratios of the beams since the BEARS receiver is operated in DSB mode. To calibrate the different intensity scales, we used calibration data obtained from the observations toward W3 and Orion IRC 2 using another SIS receiver, S100, with a single sideband (SSB) filter and acousto-optical spectrometers (AOSs). The intensity scales between the S100 receiver and the BEARS 25 beams were estimated to be 1.96–3.96 for  $^{13}\text{CO}$  and 1.57–2.77 for  $\text{C}^{18}\text{O}$ .

Our mapping observations were made with the on-the-fly (OTF) mapping technique (Sawada et al. 2008). We used an emission-free area  $\sim 2^\circ$  away from the mapping area as the off positions. We obtained OTF maps with two different scanning directions along the RA or Dec axes covering the  $20' \times 20'$  or the  $20' \times 10'$  regions, and combined them into a single map to reduce the scanning effects as much as possible. We adopted a spheroidal function<sup>1</sup> (Sawada et al. 2008) to calculate the

<sup>1</sup> Schwab (1984) is a convolution kernel and Sawada et al. (2008) described the details of the spheroidal function. We applied the parameters  $m = 6$  and  $\alpha = 1$ , which define the shape of the function.

**Table 1.** Parameters of our observations.

Molecular line	$^{13}\text{CO}$ ( $J = 1-0$ )	$\text{C}^{18}\text{O}$ ( $J = 1-0$ )
Rest frequency [GHz]	110.201354	109.782176
Observation	2013 May	2010 March–2013 May
Scan mode	OTF	OTF
Mapping size [deg $^2$ ]	0.4	0.4
Effective beam size [ $''$ ]	25.8	25.8
Velocity resolution [km s $^{-1}$ ]	0.3	0.3
Typical noise level in $T_{\text{MB}}$ [K]	0.7	0.2

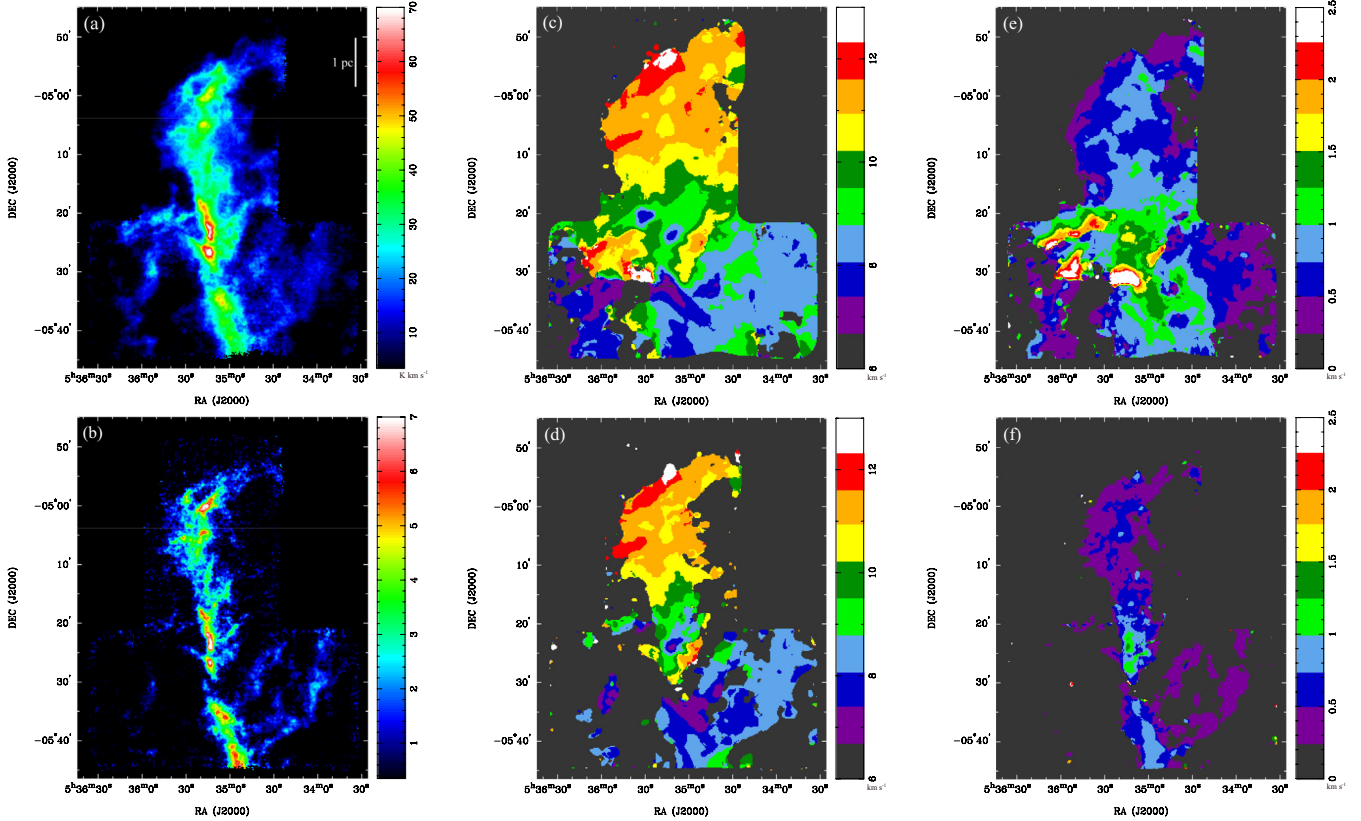


**Fig. 2.** Total intensity maps of the **a)**  $^{13}\text{CO}$  ( $J = 1-0$ ); and **b)**  $\text{C}^{18}\text{O}$  ( $J = 1-0$ ) emission lines integrated over the velocity range  $4.25 < V_{\text{LSR}} < 14.25$  km s $^{-1}$  in units of K km s $^{-1}$  ( $T_{\text{MB}}$ ). The other panels are the mean velocity maps of **c)**  $^{13}\text{CO}$  and **d)**  $\text{C}^{18}\text{O}$  in units of km s $^{-1}$ , and the velocity dispersion maps of **e)**  $^{13}\text{CO}$ ; and **f)**  $\text{C}^{18}\text{O}$  in units of km s $^{-1}$  calculated for the same velocity range for the total intensity maps. The  $^{13}\text{CO}$  and  $\text{C}^{18}\text{O}$  data in FITS format are available at the NRO web page via <http://www.nro.nao.ac.jp/~nro45mrt/html/results/data.html> and at the CDS.

intensity at each grid point of the final cube data with a spatial grid size of  $10''$ , resulting in the final effective resolution of  $25''.8$ . The  $1\sigma$  noise level of the final data is 0.5 K for  $^{13}\text{CO}$  and 0.14 K for  $\text{C}^{18}\text{O}$  in  $T_{\text{MB}}$  at a velocity resolution of 0.8 km s $^{-1}$ . By combining scans along the RA and Dec directions, we minimized the so-called scanning effect using the Emerson & Graeve (1988) PLAIT algorithm. We summarize the parameters for the  $^{13}\text{CO}$  ( $J = 1-0$ ) and  $\text{C}^{18}\text{O}$  ( $J = 1-0$ ) line observations in Table 1.

### 3. Results

#### 3.1. Distributions of the $^{13}\text{CO}$ ( $J = 1-0$ ) and $\text{C}^{18}\text{O}$ ( $J = 1-0$ ) emission lines

Figures 2a and b show the total intensity maps of the  $^{13}\text{CO}$  ( $J = 1-0$ ) and  $\text{C}^{18}\text{O}$  ( $J = 1-0$ ) emission lines, respectively, integrated over a velocity range  $4.25 < V_{\text{LSR}} < 14.25$  km s $^{-1}$

in the northern part of the Orion-A GMC. The overall distributions of the  $^{13}\text{CO}$  and  $\text{C}^{18}\text{O}$  emission lines are found to be similar to that of the  $^{12}\text{CO}$  ( $J = 1-0$ ) emission line by (Shimajiri et al. 2011). In the  $^{13}\text{CO}$  map, the brightest position is at (RA, Dec) = ( $5^{\text{h}}35^{\text{m}}13^{\text{s}}.0$ ,  $-5^{\circ}26'48''.24$ ), which is located on the western side of the Orion bar and is close to the peak position of the [CI] emission (Shimajiri et al. 2013). On the other hand, the peak position in the  $\text{C}^{18}\text{O}$  map is at (RA, Dec) = ( $5^{\text{h}}35^{\text{m}}15^{\text{s}}.7$ ,  $-5^{\circ}22'00''.24$ ) and is different from the brightest position in the  $^{13}\text{CO}$  map. The elongated structure along the north-south direction is a part of the integral-shaped filament observed in the dust-continuum emissions at  $850\ \mu\text{m}$  (Johnstone & Bally 1999), 1.2 mm (Davis et al. 2009), and 1.3 mm (Chini et al. 1997) as well as in molecular lines such as  $^{13}\text{CO}$  ( $J = 1-0$ ),  $\text{C}^{18}\text{O}$  ( $J = 1-0$ ), CS ( $J = 1-0$ ) (Tatematsu et al. 1993), and  $\text{H}^{13}\text{CO}^+$  ( $J = 1-0$ ) (Ikeda et al. 2007). We note that the size of our mapping area centered at the filament

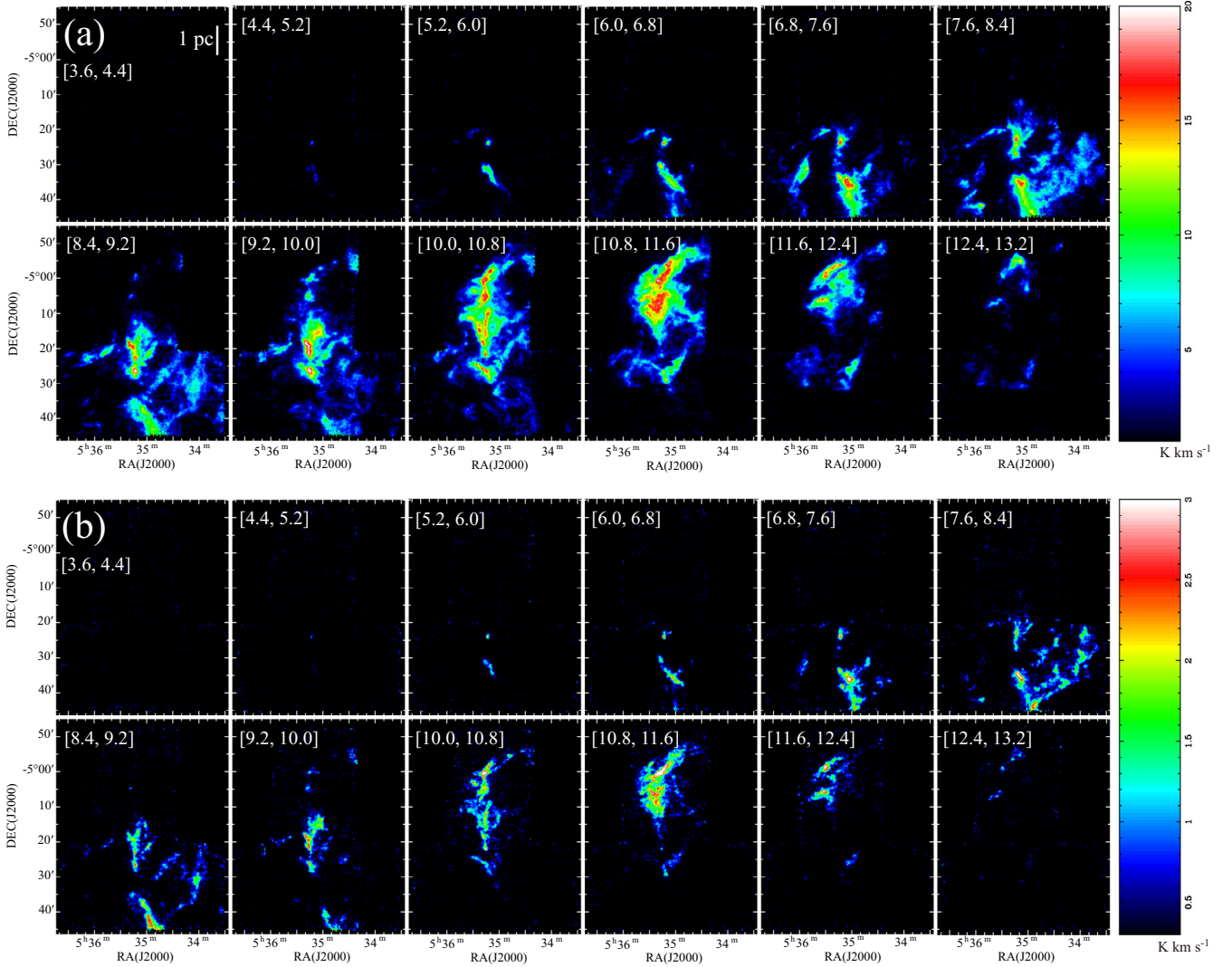


**Fig. 3.** Velocity channel maps of the **a)**  $^{13}\text{CO}$  ( $J = 1-0$ ); and **b)**  $\text{C}^{18}\text{O}$  ( $J = 1-0$ ) emission line in units of  $\text{K km s}^{-1}$  ( $T_{\text{MB}} \text{ dV}$ ). The velocity range used for the integration is indicated in the top-left corner of each panel.

is  $\sim 40'$  in the east-west direction, wider than those of the previous observations in the  $^{13}\text{CO}$  and  $\text{C}^{18}\text{O}$  ( $J = 1-0$ ) lines by (Tatematsu et al. 1993). There is a branch of the  $^{13}\text{CO}$  and  $\text{C}^{18}\text{O}$  emissions extending toward the southeast of Ori-KL. This structure, called a dark lane south filament, corresponds to one of the PDRs (Rodríguez-Franco et al. 2001; Shimajiri et al. 2011). Moreover, a bending filamentary structure with a length of  $\sim 3$  pc, is seen to the southwest of Ori-KL (also see Fig. 5). These features are also found in our previous observations in the 1.1 mm dust continuum and  $^{12}\text{CO}$  ( $J = 1-0$ ) emissions (Shimajiri et al. 2011). Hereafter, following Shimajiri et al. (2011), we call these structures the DLSF and the bending structure.

### 3.2. Velocity structures of the $^{13}\text{CO}$ and $\text{C}^{18}\text{O}$ emission lines

Figures 3a and b show the  $^{13}\text{CO}$  ( $J = 1-0$ ) and  $\text{C}^{18}\text{O}$  ( $J = 1-0$ ) velocity channel maps over the range  $3.6 < V_{\text{LSR}} < 13.2 \text{ km s}^{-1}$ . In the maps for  $4.4 < V_{\text{LSR}} < 9.2 \text{ km s}^{-1}$ , the  $^{13}\text{CO}$  and  $\text{C}^{18}\text{O}$  emission lines are distributed in the southern part of the mapping area. On the other hand, in the maps for  $10.0 < V_{\text{LSR}} < 13.2 \text{ km s}^{-1}$ , the emission lines are seen in the

northern part. These results found the large-scale velocity gradient ( $\sim 1 \text{ km s}^{-1} \text{ pc}^{-1}$ ), which has been seen in the previous studies in the  $^{12}\text{CO}$ ,  $^{13}\text{CO}$ ,  $\text{H}^{13}\text{CO}^+$ , and CS lines (Bally et al. 1987; Tatematsu et al. 1993; Ikeda et al. 2007; Shimajiri et al. 2011; Buckle et al. 2012). The velocity gradient from south to north is also seen in the mean velocity maps<sup>2</sup> of the  $^{13}\text{CO}$  and  $\text{C}^{18}\text{O}$  emission lines shown in Figs. 2c and d, respectively. In the maps for  $10.8 < V_{\text{LSR}} < 13.2 \text{ km s}^{-1}$ , the  $^{13}\text{CO}$  emission line shows a shell-like structure with a size of about two pc toward the south of Ori-KL. Its velocity structure does not follow the large-scale velocity gradient from south to north. The shell can also be recognized in the  $^{12}\text{CO}$  map (see Fig. 5 in Shimajiri et al. 2011). The overall velocity structures of  $^{13}\text{CO}$  and  $\text{C}^{18}\text{O}$  are consistent with those of  $^{12}\text{CO}$  (Shimajiri et al. 2011). However, in one of the  $^{13}\text{CO}$  channel maps at  $V_{\text{LSR}} = 10.0-10.8 \text{ km s}^{-1}$ , a shell-like

<sup>2</sup> The mean velocity maps are produced by using the task MOMENT in MIRIAD and are calculated using the equation  $\bar{V} = \int T_{\text{MB}} V dV / \int T_{\text{MB}} dV$ . We made them from the  $^{13}\text{CO}$  and  $\text{C}^{18}\text{O}$  velocity channel maps with a velocity resolution of  $0.3 \text{ km s}^{-1}$  with a clip equal to twice the respective map rms noise level. The  $1\sigma$  noise levels of the  $^{13}\text{CO}$  and  $\text{C}^{18}\text{O}$  velocity channel maps are  $0.7 \text{ K}$  and  $0.2 \text{ K}$  in units of  $T_{\text{MB}}$ .

**Table 2.** Comparison of velocity dispersion between Orion-A GMC and L1551.

Molecular line	Orion-A GMC	L 1551
$^{13}\text{CO} (J = 1-0)$	$0.67 \pm 0.34 \text{ km s}^{-1}$	$0.22 \pm 0.09 \text{ km s}^{-1}$
$\text{C}^{18}\text{O} (J = 1-0)$	$0.53 \pm 0.21 \text{ km s}^{-1}$	$0.13 \pm 0.05 \text{ km s}^{-1}$

feature centered at (RA, Dec) = ( $5^{\text{h}}34^{\text{m}}47^{\text{s}}$ ,  $-5^{\circ}32'24''$ ) can be recognized, and this feature is not obvious in the  $^{12}\text{CO}$  and  $\text{C}^{18}\text{O}$  maps.

Figures 2e and f show the velocity dispersion maps<sup>3</sup> of the  $^{13}\text{CO} (J = 1-0)$  and  $\text{C}^{18}\text{O} (J = 1-0)$  emission lines calculated over the velocity range  $5.2 < V_{\text{LSR}} < 14.0 \text{ km s}^{-1}$ . The mean values of the  $^{13}\text{CO}$  and  $\text{C}^{18}\text{O}$  velocity dispersions in the observed area are  $0.67 \pm 0.34 \text{ km s}^{-1}$  (min:  $0.30 \text{ km s}^{-1}$ , max:  $3.6 \text{ km s}^{-1}$ ) and  $0.53 \pm 0.21 \text{ km s}^{-1}$  (min:  $0.30 \text{ km s}^{-1}$ , max:  $2.8 \text{ km s}^{-1}$ ), respectively. In Table 2, we compare the velocity dispersions in the Orion-A GMC and a low-mass star-forming region, L 1551 (Yoshida et al. 2010). The velocity dispersions in the Orion-A GMC are three to four times larger than those in L 1551. Both the  $^{13}\text{CO}$  and  $\text{C}^{18}\text{O}$  velocity dispersion maps show that the velocity dispersion becomes the largest in the OMC 1 region. In addition, the velocity dispersion in the integral-shaped filament is relatively high compared with that in the outer region of the filament. The  $^{12}\text{CO}$  velocity dispersion increases toward the east of the OMC-2/3 filament (see Fig. 7 in Shimajiri et al. 2011). However, these increments in the  $^{13}\text{CO}$  and  $\text{C}^{18}\text{O}$  velocity dispersions are not recognized in our maps.

### 3.3. Column densities of the $^{13}\text{CO}$ and $\text{C}^{18}\text{O}$ gas and the abundance ratio of $^{13}\text{CO}$ to $\text{C}^{18}\text{O}$

Previous studies in the Orion-A GMC revealed that the mean density values,  $\bar{n}$ , of the filaments traced in  $^{13}\text{CO}$  and the dense cores traced in  $\text{C}^{18}\text{O}$  are  $\sim 2 \times 10^3 \text{ cm}^{-3}$  and  $\sim 5 \times 10^3 \text{ cm}^{-3}$ , respectively, assuming a cylinder and sphere (Nagahama et al. 1998; Ikeda & Kitamura 2009). These values are comparable to the critical densities of the  $^{13}\text{CO}$  and  $\text{C}^{18}\text{O} (J = 1-0)$  lines, validating the local thermodynamic equilibrium (LTE) assumption. We estimated the column densities of  $^{13}\text{CO}$  and  $\text{C}^{18}\text{O}$  on the assumption that the rotational levels of the  $^{13}\text{CO}$  and  $\text{C}^{18}\text{O}$  gas are in the LTE. The optical depths and column densities of these molecules,  $\tau_X$  and  $N_X$  where  $X = ^{13}\text{CO}$  and  $\text{C}^{18}\text{O}$ , can be derived using the equations (e.g., Kawamura et al. 1998)

$$\tau_{^{13}\text{CO}} = -\ln \left\{ 1 - \frac{T_{\text{MB}}(^{13}\text{CO})/\phi_{^{13}\text{CO}}}{5.29[J(T_{\text{ex}}) - 0.164]} \right\}, \quad (1)$$

$$N_{^{13}\text{CO}} = 2.42 \times 10^{14} \left\{ \frac{\tau_{^{13}\text{CO}} \Delta V(^{13}\text{CO}) T_{\text{ex}}}{1 - \exp[-5.29/T_{\text{ex}}]} \right\} \text{ cm}^{-2}, \quad (2)$$

$$\tau_{\text{C}^{18}\text{O}} = -\ln \left\{ 1 - \frac{T_{\text{MB}}(\text{C}^{18}\text{O})/\phi_{\text{C}^{18}\text{O}}}{5.27[J(T_{\text{ex}}) - 0.1666]} \right\}, \quad (3)$$

and

$$N_{\text{C}^{18}\text{O}} = 2.42 \times 10^{14} \left\{ \frac{\tau_{\text{C}^{18}\text{O}} \Delta V(\text{C}^{18}\text{O}) T_{\text{ex}}}{1 - \exp[-5.27/T_{\text{ex}}]} \right\} \text{ cm}^{-2}, \quad (4)$$

<sup>3</sup> The velocity dispersion maps are produced by using the task MOMENT in MIRIAD and are calculated using the equation  $\sigma^2 = \int T_{\text{MB}}(V - \bar{V})dV / \int T_{\text{MB}}dV$ . We made them from the  $^{13}\text{CO}$  and  $\text{C}^{18}\text{O}$  velocity channel maps with a velocity resolution of  $0.3 \text{ km s}^{-1}$  with a clip equal to twice the respective map rms noise level.

where  $T_{\text{ex}}$  is the excitation temperature of these molecules in K, and  $J[T] = 1/(\exp[5.29/T] - 1)$  for  $^{13}\text{CO}$  and  $J[T] = 1/(\exp[5.27/T] - 1)$  for  $\text{C}^{18}\text{O}$ . The beam filling factors of  $\phi_{^{13}\text{CO}}$  and  $\phi_{\text{C}^{18}\text{O}}$  for  $^{13}\text{CO}$  and  $\text{C}^{18}\text{O}$ , respectively, are assumed to be 1.0 (also see Sect. 4.2.1). Here, Eqs. (2) and (4) assume that the line profile can be approximated by a Gaussian function. The peak brightness temperature,  $T_{\text{MB}}$ , and the FWHM line widths,  $\Delta V (^{13}\text{CO})$  and  $\Delta V (\text{C}^{18}\text{O})$  are in units of K and  $\text{km s}^{-1}$ , respectively. We derived  $T_{\text{MB}}$  and  $\Delta V$  by fitting a Gaussian to the observed spectrum at each pixel. We considered the peak brightness temperature of  $^{12}\text{CO} (J = 1-0)$ ,  $T_{\text{CO peak}}$ , at each position (Fig. 1) as the  $T_{\text{ex}}$  values of  $^{13}\text{CO}$  and  $\text{C}^{18}\text{O}$ , assuming that the  $^{12}\text{CO}$  emission is optically thick and that the  $^{12}\text{CO}$  lines are not self-absorbed by cold foreground gas. The range of  $T_{\text{CO peak}}$  is from 12.7 K to 108.0 K and the mean value is 35.0 K.

For the pixels having signal-to-noise ratios greater than 8, we derived the optical depths and the column densities as shown in Fig. 4. The optical depths of the  $^{13}\text{CO}$  and  $\text{C}^{18}\text{O}$  lines are estimated to be  $0.05 < \tau_{^{13}\text{CO}} < 1.54$  and  $0.01 < \tau_{\text{C}^{18}\text{O}} < 0.18$ , respectively (see Figs. 4a and b). The  $\text{C}^{18}\text{O}$  emission is optically thin for most of the observed region. Although the column density of the Orion-A GMC is high, molecules in the  $J = 1-0$  transition lines become optically thin owing to the high temperature of  $>20$  K. In the northern and southern parts of the mapping area where the temperature is relatively low, the optical depths are relatively thick. In contrast, in the central part where the temperature is large, the optical depth becomes small. The column densities of the  $^{13}\text{CO}$  and  $\text{C}^{18}\text{O}$  gas are estimated to be  $0.2 \times 10^{16} < N_{^{13}\text{CO}} < 3.7 \times 10^{17}$  and  $0.4 \times 10^{15} < N_{\text{C}^{18}\text{O}} < 3.5 \times 10^{16} \text{ cm}^{-2}$ , respectively. The column density around Ori-KL is high owing to the high temperature (above 100 K) in spite of the small optical depth. In contrast, the column density in the northern and southern parts is relatively low owing to the low temperature (below 50 K) in spite of the relatively large optical depth. We summarize these values in Table 3.

Because the fractional abundances of  $^{13}\text{CO}$  ( $X_{^{13}\text{CO}} = N_{^{13}\text{CO}}/N_{\text{H}_2}$ ) and  $\text{C}^{18}\text{O}$  ( $X_{\text{C}^{18}\text{O}} = N_{\text{C}^{18}\text{O}}/N_{\text{H}_2}$ ) are proportional to their column densities, their abundance ratio can be derived as  $X_{^{13}\text{CO}}/X_{\text{C}^{18}\text{O}} = N_{^{13}\text{CO}}/N_{\text{C}^{18}\text{O}}$ . Based on the observed column densities, we found that the abundance ratio varies in the range of  $5.7 < X_{^{13}\text{CO}}/X_{\text{C}^{18}\text{O}} < 33.0$  within the observed area. The  $X_{^{13}\text{CO}}/X_{\text{C}^{18}\text{O}}$  distribution in Fig. 5a clearly shows that the ratio becomes higher in the nearly edge-on PDRs and the outskirts of the cloud. In the OMC-1, OMC-2/3, bending structure, and OMC-4 regions, the mean abundance ratio is  $12.29 \pm 0.02$  (see also Fig. 5b). On the other hand, in the nearly edge-on PDRs of the Orion-Bar, and the DLSF, and the outskirts of the cloud, the abundance ratio exceeds 15. The abundance ratio in each region is summarized in Table 4.

## 4. Discussion

### 4.1. Selective FUV photodissociation of $\text{C}^{18}\text{O}$

The significant difference between the abundance ratios of  $X_{^{13}\text{CO}}/X_{\text{C}^{18}\text{O}}$  in the PDRs and the other regions are clearly demonstrated in the correlation diagrams between the column densities of  $^{13}\text{CO}$  and  $\text{C}^{18}\text{O}$  in Fig. 6. In OMC-1, OMC-2/3, OMC-4, and bending structure, the mean values of  $X_{^{13}\text{CO}}/X_{\text{C}^{18}\text{O}}$  are  $12.14 \pm 0.04$ ,  $12.92 \pm 0.04$ ,  $11.64 \pm 0.05$ , and  $11.68 \pm 0.04$ , respectively. On the other hand, in the PDR regions of the Orion bar and DLSF, the mean values of  $X_{^{13}\text{CO}}/X_{\text{C}^{18}\text{O}}$  are  $16.58 \pm 0.04$  and  $15.83 \pm 0.14$ , respectively. The  $X_{^{13}\text{CO}}/X_{\text{C}^{18}\text{O}}$  values of  $\sim 16$  is a factor of three larger than the value of 5.5 in the solar system

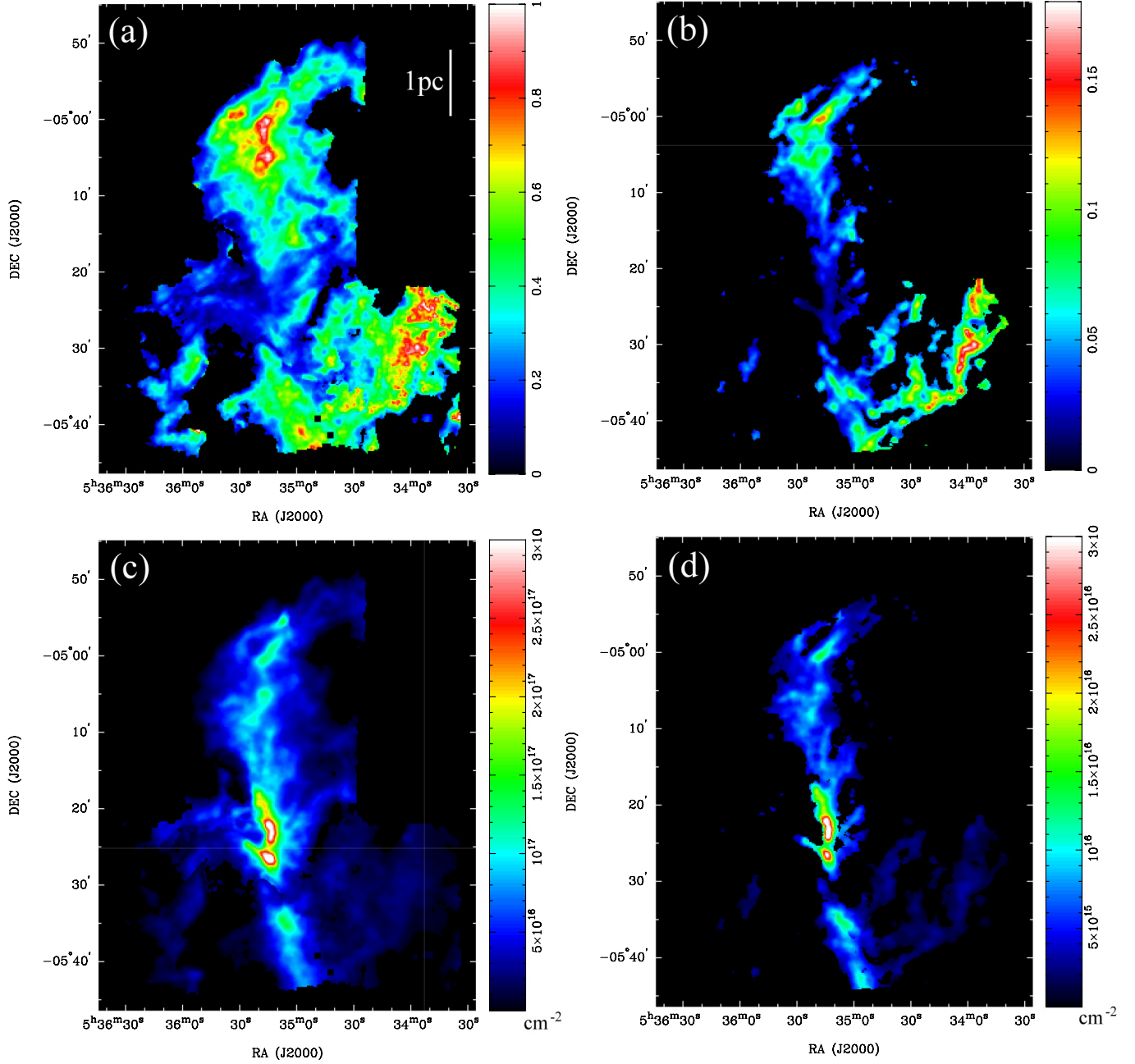


**Fig. 4.** Maps of the optical depths of the **a)**  $^{13}\text{CO}$  ( $J = 1-0$ ) and **b)**  $\text{C}^{18}\text{O}$  ( $J = 1-0$ ) emission lines, and maps of the column densities of **c)**  $^{13}\text{CO}$  and **d)**  $\text{C}^{18}\text{O}$  molecules. The optical depths and column densities are estimated on the assumption that the excitation temperatures of the  $^{13}\text{CO}$  and  $\text{C}^{18}\text{O}$  ( $J = 1-0$ ) lines are equal to the peak temperatures of the  $^{12}\text{CO}$  ( $J = 1-0$ ) emission in  $T_{\text{MB}}$  and are calculated for pixels with intensities above the  $8\sigma$  noise levels.

**Table 3.** Column densities of the  $^{13}\text{CO}$  and  $\text{C}^{18}\text{O}$  gas.

Molecule	$T_{\text{ex}}$	Beam filling factor	Optical depth	Column density
$^{13}\text{CO}$	$T_{\text{CO peak}}$	1.0	0.05–1.54	$(0.2-37.1) \times 10^{16} \text{ cm}^{-2}$
$\text{C}^{18}\text{O}$	$T_{\text{CO peak}}$	1.0	0.01–0.18	$(0.4-35.1) \times 10^{15} \text{ cm}^{-2}$
$^{13}\text{CO}$	$T_{\text{CO peak}}$	0.8	0.06–4.09	$(0.3-48.0) \times 10^{16} \text{ cm}^{-2}$
$\text{C}^{18}\text{O}$	$T_{\text{CO peak}}$	0.8	0.01–0.23	$(0.5-43.9) \times 10^{15} \text{ cm}^{-2}$
$^{13}\text{CO}$	30 K	1.0	0.05–1.53	$(0.3-22.1) \times 10^{16} \text{ cm}^{-2}$
$\text{C}^{18}\text{O}$	20 K	1.0	0.02–0.29	$(0.5-9.9) \times 10^{15} \text{ cm}^{-2}$
$^{13}\text{CO}$	30 K	0.8	0.06–3.91	$(0.4-55.0) \times 10^{16} \text{ cm}^{-2}$
$\text{C}^{18}\text{O}$	20 K	0.8	0.03–0.38	$(0.6-12.7) \times 10^{15} \text{ cm}^{-2}$

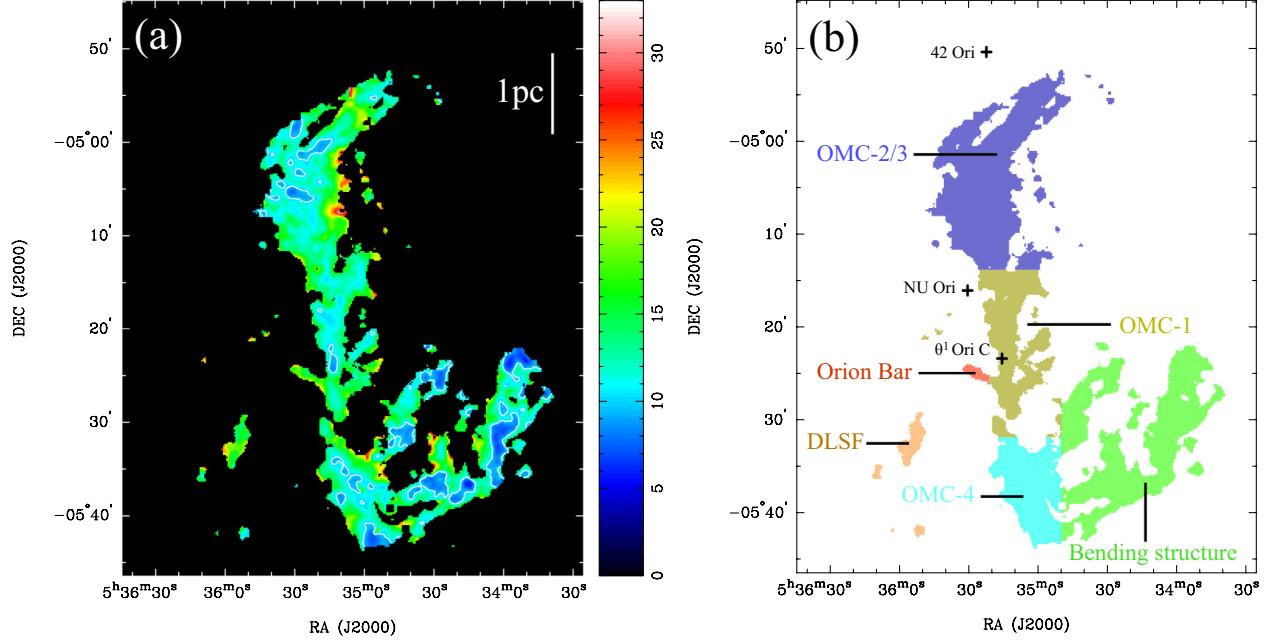


**Fig. 5.** **a)** Map of the abundance ratio  $X_{^{13}\text{CO}}/X_{\text{C}^{18}\text{O}}$ . **b)** Locations of the regions summarized in Table 4. Colors to indicate the individual regions are the same as those of the plots in Fig. 6. In panel **a)**, the contours show the value of  $X_{^{13}\text{CO}}/X_{\text{C}^{18}\text{O}} = 10$ . The crosses show the positions of  $\theta^1$  Ori C, NU Ori, and 42 Ori, which are the exciting stars of the HII regions, M 42, M 43, and NGC 1977.

**Table 4.** Abundance ratio  $X_{^{13}\text{CO}}/X_{\text{C}^{18}\text{O}}$  in the six distinct regions.

$T_{\text{ex } ^{13}\text{CO}}$	$T_{\text{ex } \text{C}^{18}\text{O}}$	$\phi_{^{13}\text{CO}}$	$\phi_{\text{C}^{18}\text{O}}$	Orion Bar	DLSF	OMC-1	OMC-2/3	OMC-4	Bending structure
$T_{\text{CO peak}}$	$T_{\text{CO peak}}$	1.0	1.0	$16.58 \pm 0.17$	$15.83 \pm 0.14$	$12.14 \pm 0.04$	$12.92 \pm 0.04$	$11.64 \pm 0.05$	$11.68 \pm 0.04$
$T_{\text{CO peak}}$	$T_{\text{CO peak}}$	1.0	0.8	$13.25 \pm 0.14$	$12.61 \pm 0.12$	$9.68 \pm 0.03$	$10.26 \pm 0.03$	$9.25 \pm 0.04$	$9.25 \pm 0.03$
$T_{\text{CO peak}}$	$T_{\text{CO peak}}$	0.8	0.8	$16.90 \pm 0.18$	$16.80 \pm 0.16$	$12.53 \pm 0.04$	$14.06 \pm 0.04$	$12.46 \pm 0.05$	$12.61 \pm 0.04$
30 K	20 K	1.0	1.0	$27.45 \pm 0.25$	$22.82 \pm 0.21$	$20.23 \pm 0.07$	$18.78 \pm 0.06$	$16.25 \pm 0.08$	$14.12 \pm 0.05$
30 K	20 K	1.0	0.8	$21.79 \pm 0.20$	$18.09 \pm 0.17$	$15.99 \pm 0.05$	$14.76 \pm 0.05$	$12.81 \pm 0.06$	$11.18 \pm 0.04$
30 K	20 K	0.8	0.8	$30.27 \pm 0.28$	$25.14 \pm 0.25$	$24.31 \pm 0.11$	$22.17 \pm 0.07$	$18.08 \pm 0.10$	$14.59 \pm 0.06$
Number of pixels				108	371	2673	5487	2150	5061

(Wilson & Matteucci 1992). It should represent the chemical difference between the PDRs and the other regions. The chemical difference between the PDR and the other regions is likely to be caused by the different FUV intensities around the regions. Since the FUV intensities around the PDR regions are considerably higher than those around the other regions, the selective UV photodissociation of  $\text{C}^{18}\text{O}$  (Yurimoto & Kuramoto 2004; Lada et al. 1994) efficiently occurs over the entire PDR region. Thus, the  $X_{^{13}\text{CO}}/X_{\text{C}^{18}\text{O}}$  value should be higher in the PDRs.

The interstellar UV radiation probably also causes the selective UV photodissociation of  $\text{C}^{18}\text{O}$  in the outskirts of the cloud. Figures 7d–g show that the  $X_{^{13}\text{CO}}/X_{\text{C}^{18}\text{O}}$  ratios at low column densities are as high as the ratios in the PDRs, while the ratios decrease with increasing column densities. The theoretical study predicts that the  $X_{^{13}\text{CO}}/X_{\text{C}^{18}\text{O}}$  ratio reaches values between 5 and 10 in regions with  $A_V = 1\text{--}3$  (Warin et al. 1996). The  $X_{^{13}\text{CO}}/X_{\text{C}^{18}\text{O}}$  values at low column densities in the OMC-1, OMC-2/3, OMC-4, and bending structure regions are, however, higher than the predicted values of 5 to 10. The reason might be that these regions are influenced by the FUV radiation from OB stars embedded in the Orion-A GMC such as the NGC 1977, M 43, and Trapezium cluster ( $\theta^1$  Ori C), as well as the interstellar UV radiation. In OMC-1, which is the closest region to the Trapezium cluster ( $\theta^1$  Ori C), the  $X_{^{13}\text{CO}}/X_{\text{C}^{18}\text{O}}$  ratios are

higher than those at the same  $N_{\text{C}^{18}\text{O}}$  column density in OMC-2/3, OMC-4, and bending structure, although the ratios decrease with increasing column densities.

In addition, the  $X_{^{13}\text{CO}}/X_{\text{C}^{18}\text{O}}$  ratio remains high even at larger  $A_V$  values than the theoretically predicted values of 1 to 3 mag (Warin et al. 1996). We can estimate the  $A_V$  value from the column density  $N_{\text{C}^{18}\text{O}}$  by using the following relation derived in the Taurus region by Frerking et al. (1982):

$$A_V = \frac{N_{\text{C}^{18}\text{O}} (\text{cm}^{-2})}{2.4 \times 10^{14}} + 2.9. \quad (5)$$

Thus, the value of  $N_{\text{C}^{18}\text{O}} = 4.0 \times 10^{14} \text{ cm}^{-2}$ , which is the lowest value of the  $\text{C}^{18}\text{O}$  column density in the observed area, corresponds to the value of  $A_V = 4.5$  mag. We note that this value of  $A_V$  should be the lower limit, because the  $\text{C}^{18}\text{O}$  molecules are likely to be selectively dissociated by the FUV radiation. We conclude that the FUV radiation penetrates the innermost part of the cloud and the whole of our observed region is chemically influenced by the FUV radiation from the OB stars embedded in the Orion-A GMC.

The chemical fractionation of  $^{13}\text{C}^+ + ^{12}\text{CO} \rightarrow ^{13}\text{CO} + ^{12}\text{C}^+$  ( $\Delta E = 35$  K) is considered to occur at the cloud surface (Langer et al. 1984). The selective photodissociation of  $\text{C}^{18}\text{O}$  is, however, thought to be more dominant than the chemical

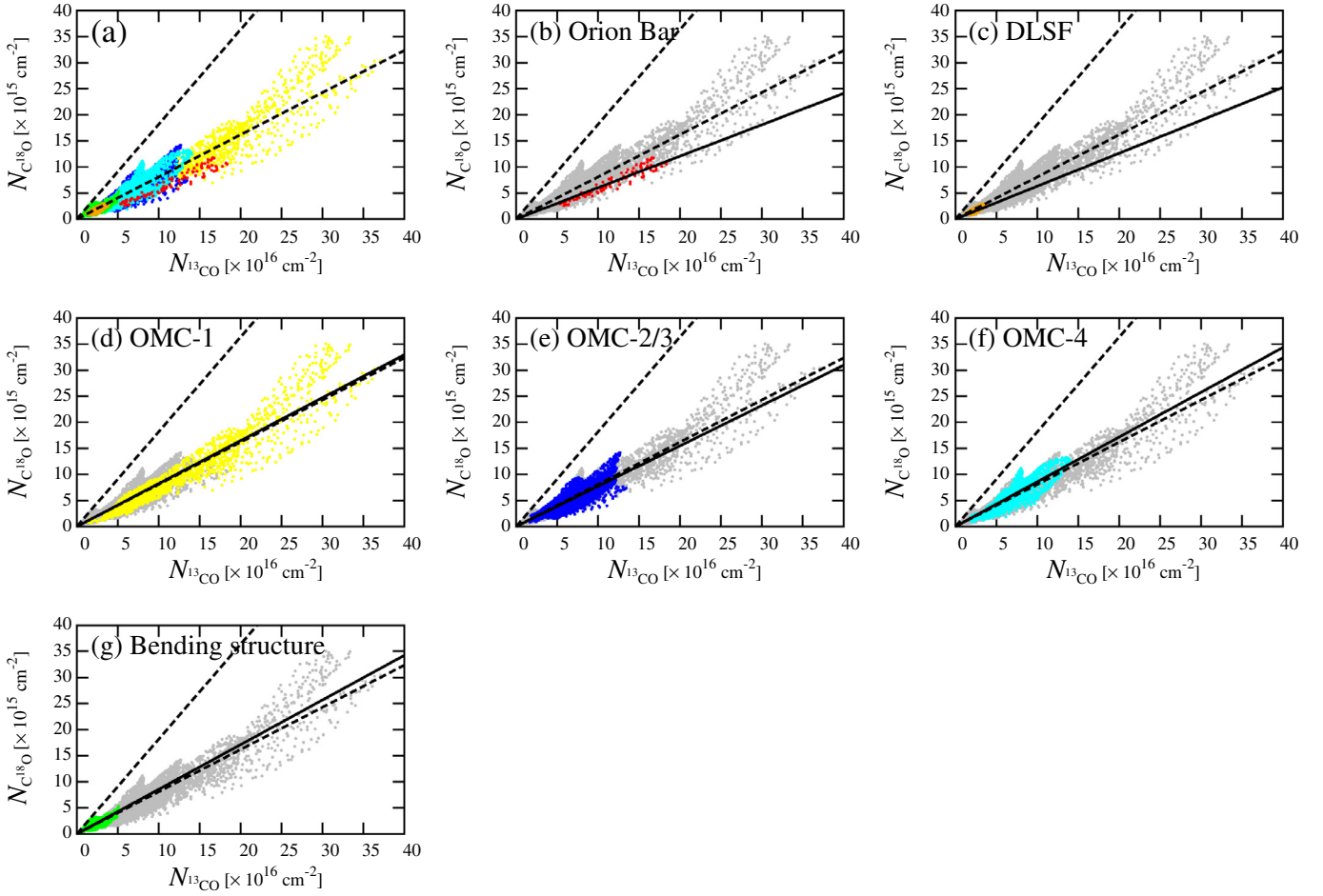


**Fig. 6.**  $N_{13\text{CO}}$  vs.  $N_{\text{C}^{18}\text{O}}$  measured in **a)** the entire region; **b)** the Orion Bar, **c)** DLSF; **d)** OMC-1; **e)** OMC-2/3; **f)** OMC-4; and **g)** bending structure area, respectively. The gray, red, orange, yellow, blue, aqua, and green plots are taken from the entire region, data points in the Orion bar, DLSF, OMC-1, OMC-2/3, OMC-4, and bending structure, respectively. The black dashed lines indicate  $X_{13\text{CO}}/X_{\text{C}^{18}\text{O}} = 5.5$  and  $12.3$ . In panels **b)–g)**, black lines denote the best fitting lines to measure the abundance ratio  $X_{13\text{CO}}/X_{\text{C}^{18}\text{O}}$  for each region (see Table 4).

fractionation, because the temperature of the low column density areas ( $N_{\text{C}^{18}\text{O}} < 5 \times 10^{15} \text{ cm}^{-2}$ ) of the Orion-A GMC is high ( $T_{\text{ex}} = 28.4 \pm 9.7 \text{ K}$ ).

#### 4.2. Influence of the uncertainties in the beam filling factor and the excitation temperature on our derived abundance ratio of $^{13}\text{CO}$ to $\text{C}^{18}\text{O}$

##### 4.2.1. Influence of the beam filling factor

In Sect. 3.3, we derived the optical depths and column densities of  $^{13}\text{CO}$  and  $\text{C}^{18}\text{O}$  by using Eqs. (1)–(4) assuming that the emitting region fills the beam, i.e., the beam filling factors,  $\phi_{13\text{CO}}$  and  $\phi_{\text{C}^{18}\text{O}}$ , are 1.0. Here, we investigate the influence of the beam filling factor on the derived physical properties.

According to Nummelin et al. (1998) and Kim et al. (2006), we can estimate the beam filling factor by the equation

$$\phi = \frac{\theta_{\text{source}}^2}{\theta_{\text{source}}^2 + \theta_{\text{beam}}^2}, \quad (6)$$

where  $\theta_{\text{source}}$  and  $\theta_{\text{beam}}$  are the source and beam sizes, respectively. The effective beam size of the  $^{13}\text{CO}$  and  $\text{C}^{18}\text{O}$  data is  $25.8''$ , which corresponds to  $0.05 \text{ pc}$  at the distance of the Orion-A GMC. The sizes of the structures traced by the  $^{13}\text{CO}$  and  $\text{C}^{18}\text{O}$  emission lines in the Orion-A GMC can be estimated

from previous observations. The  $\text{C}^{18}\text{O}$  emission is thought to trace the dense cores, clumps, and/or filaments. On the other hand, the  $^{13}\text{CO}$  emission is likely to trace more extended components than the  $\text{C}^{18}\text{O}$  emission as seen in the integrated intensity maps (Figs. 2a and b). Previous observations toward the Orion-A GMC in  $\text{H}^{13}\text{CO}^+$  (1–0) using the Nobeyama 45 m telescope identified 236 dense cores with the clumpfind algorithm (Ikeda et al. 2007). They estimated the size corrected for the antenna-beam size on the assumption of a Gaussian intensity profile and revealed that the typical size of dense cores traced in  $\text{H}^{13}\text{CO}^+$  is  $0.14 \text{ pc}$ . The sizes of the dense cores traced in  $\text{C}^{18}\text{O}$  are expected to exceed  $0.14 \text{ pc}$ , since the critical density of  $\text{H}^{13}\text{CO}^+$  is higher than that of  $\text{C}^{18}\text{O}$ . As a reference, previous observations toward the Taurus cloud, which is one of the nearest low-mass star forming regions ( $d = 140 \text{ pc}$ , Elias 1978), revealed that the typical size of the dense cores traced in  $\text{C}^{18}\text{O}$  is  $0.1 \text{ pc}$  (Onishi et al. 1996). Furthermore, the Herschel observations in the  $70 \mu\text{m}$ ,  $160 \mu\text{m}$ ,  $250 \mu\text{m}$ ,  $350 \mu\text{m}$ , and  $500 \mu\text{m}$  emissions revealed the omnipresence of parsec-scale filaments in molecular clouds and found that the filaments have very narrow widths: a typical FWHM value of  $0.1 \text{ pc}$  (Arzoumanian et al. 2011; Palmeirim et al. 2013). From the above, the sizes of the dense cores, clumps, and/or filaments traced in  $^{13}\text{CO}$  and  $\text{C}^{18}\text{O}$  are expected to exceed  $0.1 \text{ pc}$ . In the case of our observations, the beam filling factor is expected to exceed  $0.8$  on the assumption

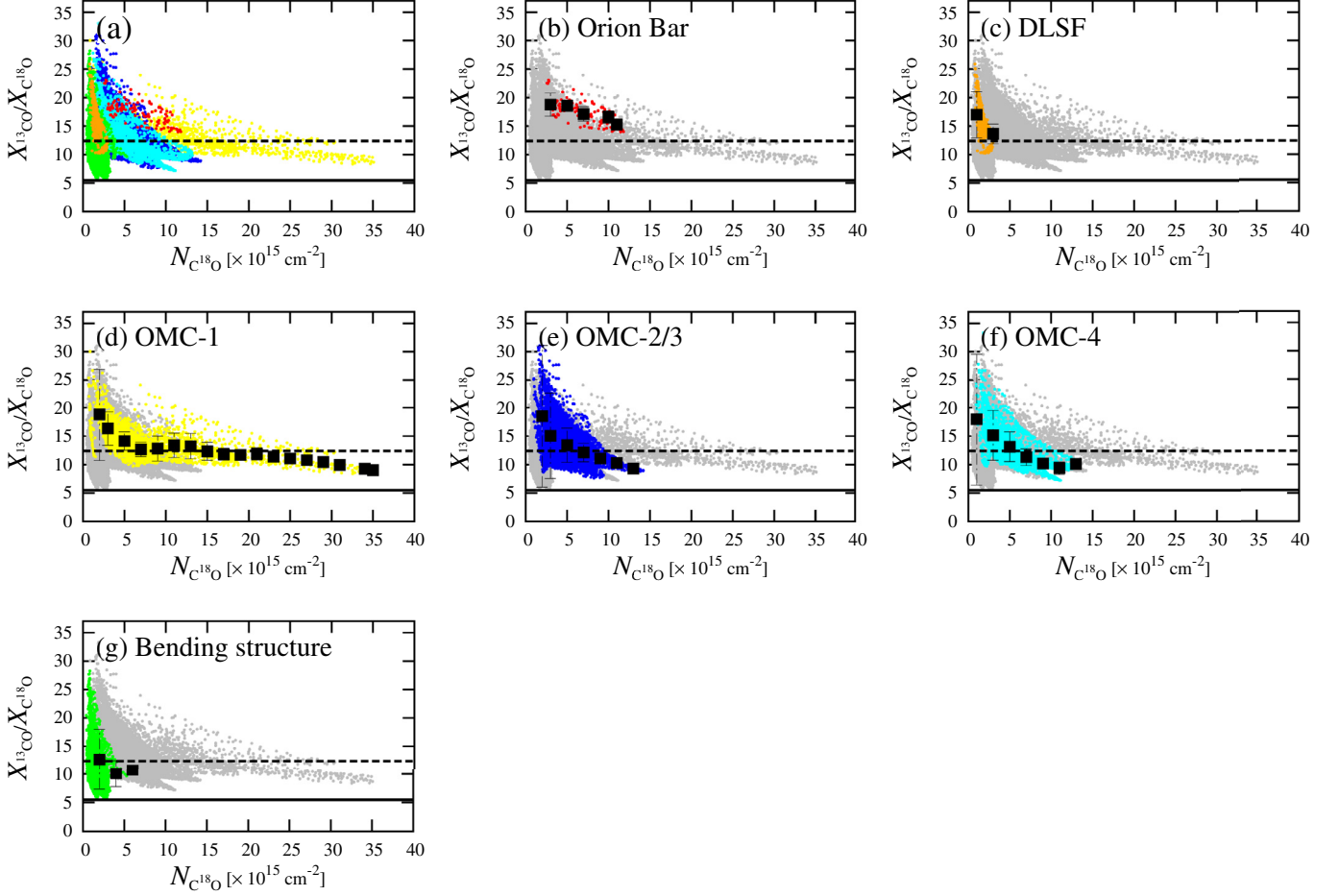


**Fig. 7.**  $N_{\text{C}^{18}\text{O}}$  vs.  $X_{^{13}\text{CO}}/X_{\text{C}^{18}\text{O}}$  measured in **a)** the entire region; **b)** the Orion Bar; **c)** DLSF, **d)** OMC-1; **e)** OMC-2/3; **f)** OMC-4; and **g)** bending structure area, respectively. The gray, red, orange, yellow, blue, aqua, and green plots are taken from the entire region, data points in the Orion bar, DLSF, OMC-1, OMC-2/3, OMC-4, and bending structure, respectively. The black lines indicate  $X_{^{13}\text{CO}}/X_{\text{C}^{18}\text{O}} = 5.5$ . The dashed lines indicate  $X_{^{13}\text{CO}}/X_{\text{C}^{18}\text{O}} = 12.3$ , which is the mean value of  $X_{^{13}\text{CO}}/X_{\text{C}^{18}\text{O}}$  for the entire region. The filled squares show the mean  $X_{^{13}\text{CO}}/X_{\text{C}^{18}\text{O}}$  which is computed by binning the individually calculated ratios into intervals of  $2.0 \times 10^{15} \text{ cm}^{-2}$ . The error bars show the standard deviations in each bin.

that  $\theta_{\text{source}} > 0.1 \text{ pc}$  and  $\theta_{\text{beam}} = 0.05 \text{ pc}$ . In Tables 3 and 4, we summarize the optical depths, the column densities, and the abundance ratios of  $^{13}\text{CO}$  to  $\text{C}^{18}\text{O}$ . The  $X_{^{13}\text{CO}}/X_{\text{C}^{18}\text{O}}$  values on the assumption of  $\phi_{^{13}\text{CO}} = 1.0$  and  $\phi_{\text{C}^{18}\text{O}} = 0.8$  decrease compared with those of  $\phi_{^{13}\text{CO}} = \phi_{\text{C}^{18}\text{O}} = 1.0$ . Nevertheless, the  $X_{^{13}\text{CO}}/X_{\text{C}^{18}\text{O}}$  values in the nearly edge-on PDRs of Orion Bar and DLSF are (2.3–2.4) times larger than the solar system value. Furthermore, the  $X_{^{13}\text{CO}}/X_{\text{C}^{18}\text{O}}$  values even in the OMC-1, OMC-2/3, OMC-4, and bending structure are also (1.7–1.9) times larger than the solar system value. Even after taking into consideration of uncertainties in the beam filling factors of  $^{13}\text{CO}$  and  $\text{C}^{18}\text{O}$ , we safely conclude that the abundance ratio of  $^{13}\text{CO}$  to  $\text{C}^{18}\text{O}$  is significantly high toward the nearly edge-on PDRs in the Orion-A GMC.

#### 4.2.2. Influence of the excitation temperature

To estimate the optical depths and the column densities, we considered the  $^{12}\text{CO}$  ( $J = 1-0$ ) peak temperature in  $T_{\text{MB}}$  as the excitation temperatures of  $^{13}\text{CO}$  ( $J = 1-0$ ) and  $\text{C}^{18}\text{O}$  ( $J = 1-0$ ). There is, however, a possibility that the  $^{13}\text{CO}$  and  $\text{C}^{18}\text{O}$  lines trace colder areas than the  $^{12}\text{CO}$  line, because the  $^{13}\text{CO}$  and  $\text{C}^{18}\text{O}$  lines are optically thinner than the  $^{12}\text{CO}$  line and probably trace the inner parts of the cloud. Castets et al. (1990) found that the  $^{13}\text{CO}$  and  $\text{C}^{18}\text{O}$  line emissions trace the regions with a

temperature of 20–30 K and  $<20 \text{ K}$ , respectively, from the observations toward the Orion-A GMC in the  $^{13}\text{CO}$  ( $2-1$ ,  $1-0$ ) and  $\text{C}^{18}\text{O}$  ( $2-1$ ,  $1-0$ ) line emissions with low angular resolutions of  $100''$ – $140''$ . Therefore, in order to investigate the influence of the uncertainties in excitation temperature on the derived physical properties, we also derived the physical properties on the assumption of  $T_{\text{ex } ^{13}\text{CO}} = 30 \text{ K}$  and  $T_{\text{ex } \text{C}^{18}\text{O}} = 20 \text{ K}$ . These values are summarized in Tables 3 and 4.

The optical depths obtained with the assumption of  $T_{\text{ex } ^{13}\text{CO}} = 30 \text{ K}$  and  $T_{\text{ex } \text{C}^{18}\text{O}} = 20 \text{ K}$  are similar to those for  $T_{\text{ex}} = T_{^{12}\text{CO peak}}$ . In contrast, the column densities derived on the assumption of  $T_{\text{ex}} = T_{^{12}\text{CO peak}}$  are overestimated by a factor of 1.5–3.0. The  $X_{^{13}\text{CO}}/X_{\text{C}^{18}\text{O}}$  values are, however, estimated to be a factor of 1.2–1.9 larger than the values obtained with the assumption of  $T_{\text{ex}} = T_{^{12}\text{CO peak}}$ . Thus, the  $X_{^{13}\text{CO}}/X_{\text{C}^{18}\text{O}}$  values in the Orion-A GMC are (2.5–5.0) times larger than the solar system value, even after taking into consideration the uncertainties in the  $^{13}\text{CO}$  and  $\text{C}^{18}\text{O}$  ( $J = 1-0$ ) excitation temperatures.

#### 4.2.3. Robustness of the high abundance ratio of $^{13}\text{CO}$ to $\text{C}^{18}\text{O}$

Finally, we demonstrate that the high abundance ratio of  $^{13}\text{CO}$  to  $\text{C}^{18}\text{O}$  is most likely to be a direct consequence of the high intensity ratio of  $^{13}\text{CO}$  to  $\text{C}^{18}\text{O}$  in the Orion-A GMC. Figure 8

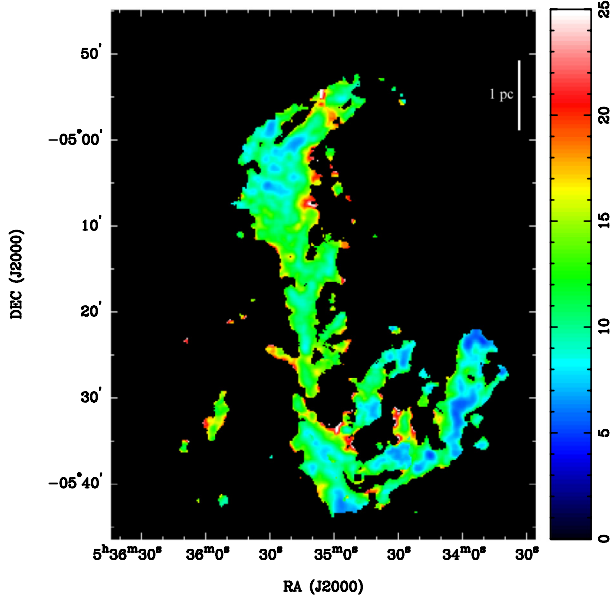


Fig. 8. Map of the integrated intensity ratio of  $^{13}\text{CO}$  to  $\text{C}^{18}\text{O}$ .

shows the distribution of the integrated intensity ratio of  $^{13}\text{CO}$  ( $J = 1-0$ ) to  $\text{C}^{18}\text{O}$  ( $J = 1-0$ ),  $R_{13,18} = I_{^{13}\text{CO}}/I_{\text{C}^{18}\text{O}}$ . The mean  $R_{13,18}$  value within the observed area is found to be  $11.4 \pm 3.2$  (min: 4.9, max: 32.3). The  $R_{13,18}$  values in the six distinct regions are summarized in Table 5. The  $R_{13,18}$  values in the nearly edge-on PDRs of the Orion Bar and DLSF seem larger than those in the other regions. The observed intensity ratio,  $R_{13,18}$ , is related with the six parameters of  $\phi_{^{13}\text{CO}}$ ,  $\phi_{\text{C}^{18}\text{O}}$ ,  $T_{\text{ex } ^{13}\text{CO}}$ ,  $T_{\text{ex } \text{C}^{18}\text{O}}$ ,  $\tau_{^{13}\text{CO}}$ , and  $X_{^{13}\text{CO}}/X_{\text{C}^{18}\text{O}}$  ( $=A_{13,18}$ ) as follows:

$$R_{13,18} = \frac{\phi_{^{13}\text{CO}}}{\phi_{\text{C}^{18}\text{O}}} \frac{1 - \exp(-\tau_{^{13}\text{CO}})}{1 - \exp(-\tau_{^{13}\text{CO}}/A_{13,18})} \times \frac{5.29[J(T_{\text{ex } ^{13}\text{CO}}) - 0.164]}{5.27[J(T_{\text{ex } \text{C}^{18}\text{O}}) - 0.1666]} \quad (7)$$

Figure 9 shows contour maps of  $R_{13,18}$  in the  $\tau_{^{13}\text{CO}} - X_{^{13}\text{CO}}/X_{\text{C}^{18}\text{O}}$  plane for the minimum and maximum values of the coefficient of  $\phi_{^{13}\text{CO}}/\phi_{\text{C}^{18}\text{O}} \times J(T_{\text{ex } ^{13}\text{CO}})/J(T_{\text{ex } \text{C}^{18}\text{O}})$  in Eq. (7). The  $R_{13,18}$  value increases with the increasing abundance ratio, if  $\tau_{^{13}\text{CO}} < \sim 1$ . To explain the mean  $R_{13,18}$  value of 11.4 within the observed area, the lower limits of the abundance ratio,  $X_{^{13}\text{CO}}/X_{\text{C}^{18}\text{O}}$ , are 11.5 for the maximum case in the left panel and 5.8 for the minimum case in the right panel. Furthermore, the lower limits of the  $X_{^{13}\text{CO}}/X_{\text{C}^{18}\text{O}}$  values in the nearly edge-on PDRs of the Orion Bar and DLSF are 17.1 and 14.6 for the maximum case and 14.6 and 7.3 for the minimum case. In addition, the lower limits of the  $X_{^{13}\text{CO}}/X_{\text{C}^{18}\text{O}}$  values in the OMC-1, OMC-2/3, OMC-4, and bending structure are 12.6, 11.8, 11.5, and 10.1 for the maximum case and 6.3, 5.9, 5.8, and 5.4 for the minimum case. In spite of the uncertainties in our adopted parameters in Eq. (7), we conclude that the lower limits of  $X_{^{13}\text{CO}}/X_{\text{C}^{18}\text{O}}$  values in the nearly edge-on PDRs tend to be larger than those in the other regions and the  $X_{^{13}\text{CO}}/X_{\text{C}^{18}\text{O}}$  values within the observed area are (1.3–3.1) times larger than the solar system value of 5.5.

## 5. Conclusions

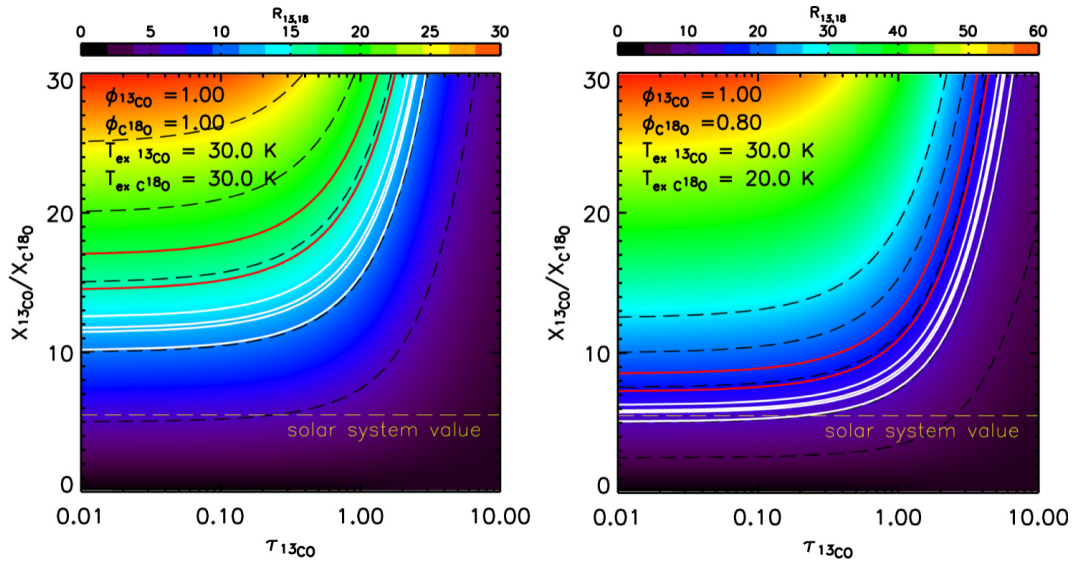
We have carried out wide-field ( $0.4 \text{ deg}^2$ ) observations with an angular resolution of  $25.8''$  ( $\sim 0.05 \text{ pc}$ ) in the  $^{13}\text{CO}$  ( $J = 1-0$ )

Table 5. Integrated intensity ratio of  $^{13}\text{CO}$  to  $\text{C}^{18}\text{O}$ .

Region	$R_{13,18}$
Orion Bar	$17.0 \pm 1.9$
DLSF	$14.5 \pm 2.7$
OMC-1	$12.5 \pm 2.5$
OMC-2/3	$11.7 \pm 3.1$
OMC-4	$11.4 \pm 3.4$
Bending structure	$10.1 \pm 3.0$
Entire region	$11.4 \pm 3.2$

and  $\text{C}^{18}\text{O}$  ( $J = 1-0$ ) emission lines toward the Orion-A GMC. The main results are summarized as follows:

1. The overall distributions and velocity structures of the  $^{13}\text{CO}$  and  $\text{C}^{18}\text{O}$  emission lines are similar to those of the  $^{12}\text{CO}$  ( $J = 1-0$ ) emission line. The  $^{13}\text{CO}$  velocity channel maps show a new shell-like structure, which is not obvious in the  $^{12}\text{CO}$  and  $\text{C}^{18}\text{O}$  maps.
2. We estimated the optical depths and column densities of the  $^{13}\text{CO}$  and  $\text{C}^{18}\text{O}$  emission lines. The optical depths of  $^{13}\text{CO}$  and  $\text{C}^{18}\text{O}$  are estimated to be  $0.05 < \tau_{^{13}\text{CO}} < 1.54$  and  $0.01 < \tau_{\text{C}^{18}\text{O}} < 0.18$ , respectively. The column densities of the  $^{13}\text{CO}$  and  $\text{C}^{18}\text{O}$  gas are estimated to be  $0.2 \times 10^{16} < N_{^{13}\text{CO}} < 3.7 \times 10^{17}$  and  $0.4 \times 10^{15} < N_{\text{C}^{18}\text{O}} < 3.5 \times 10^{16} \text{ cm}^{-2}$ , respectively.
3. The abundance ratio between  $^{13}\text{CO}$  and  $\text{C}^{18}\text{O}$ ,  $X_{^{13}\text{CO}}/X_{\text{C}^{18}\text{O}}$ , is found to be 5.7–33.0. The mean value of  $X_{^{13}\text{CO}}/X_{\text{C}^{18}\text{O}}$  of the the nearly edge-on PDRs such as the Orion Bar and DLSF are 16.5, which is a factor of three larger than the solar system value of 5.5. On the other hand, the mean value of  $X_{^{13}\text{CO}}/X_{\text{C}^{18}\text{O}}$  in the other regions is 12.3. The difference between the abundance ratios in nearly edge-on PDRs and the other regions are likely due to the different intensities of the FUV radiation that cause the selective photodissociation of  $\text{C}^{18}\text{O}$ .
4. In the low column density regions ( $N_{\text{C}^{18}\text{O}} < 5 \times 10^{15} \text{ cm}^{-2}$ ), we found that the abundance ratio exceeds 10. These regions are thought to be influenced by the FUV radiation from the OB stars embedded in the Orion-A GMC such as the NGC 1977, M 43, and Trapezium cluster as well as the interstellar UV radiation.
5. To examine the influence of the beam filling factor in our observations on the abundance ratio of  $^{13}\text{CO}$  to  $\text{C}^{18}\text{O}$ , we estimated the beam filling factors for the  $^{13}\text{CO}$  and  $\text{C}^{18}\text{O}$  gas to exceed 0.8. After taking into consideration the uncertainties in the beam filling factor, we also found the high abundance ratio  $X_{^{13}\text{CO}}/X_{\text{C}^{18}\text{O}}$  over the Orion-A cloud, particularly toward the nearly edge-on PDRs.
6. Even if we consider the lower excitation temperatures of  $T_{\text{ex } ^{13}\text{CO}} = 30 \text{ K}$  and  $T_{\text{ex } \text{C}^{18}\text{O}} = 20 \text{ K}$ , we come to the same conclusion that the abundance ratio  $X_{^{13}\text{CO}}/X_{\text{C}^{18}\text{O}}$  becomes high toward the nearly edge-on PDRs.
7. We checked the robustness of our conclusions in the Orion-A GMC by varying  $\phi_{^{13}\text{CO}}$ ,  $\phi_{\text{C}^{18}\text{O}}$ ,  $T_{\text{ex } ^{13}\text{CO}}$ ,  $T_{\text{ex } \text{C}^{18}\text{O}}$ ,  $\tau_{^{13}\text{CO}}$ , and  $X_{^{13}\text{CO}}/X_{\text{C}^{18}\text{O}}$ . To explain the mean value of 11.4 for the intensity ratio  $R_{13,18}$  in our observed region, the lower limit of the  $X_{^{13}\text{CO}}/X_{\text{C}^{18}\text{O}}$  value should be (5.8–11.5) times larger than the solar system value of 5.5. In addition, the  $X_{^{13}\text{CO}}/X_{\text{C}^{18}\text{O}}$  values in the nearly edge-on PDRs are most likely larger than those in the other regions.
8. When studying the range of possible values of the beam filling factors and of the excitation temperatures, the conclusion



**Fig. 9.** Contour maps of the integrated intensity ratio of  $^{13}\text{CO}$  to  $\text{C}^{18}\text{O}$  in the parameter plane of the optical depth of  $^{13}\text{CO}$  and the abundance ratio of  $^{13}\text{CO}$  to  $\text{C}^{18}\text{O}$ . In the *left panel*,  $\phi_{^{13}\text{CO}} = 1.0$ ,  $\phi_{\text{C}^{18}\text{O}} = 1.0$ ,  $T_{\text{ex } ^{13}\text{CO}} = 30.0 \text{ K}$ , and  $T_{\text{ex } \text{C}^{18}\text{O}} = 30.0 \text{ K}$  are assumed. In the *right panel*,  $\phi_{^{13}\text{CO}} = 1.0$ ,  $\phi_{\text{C}^{18}\text{O}} = 0.8$ ,  $T_{\text{ex } ^{13}\text{CO}} = 30.0 \text{ K}$ , and  $T_{\text{ex } \text{C}^{18}\text{O}} = 20.0 \text{ K}$  are assumed. The yellow dashed lines indicate  $X_{^{13}\text{CO}}/X_{\text{C}^{18}\text{O}} = 5.5$ , which is the solar system value. The black dashed lines indicate  $R_{^{13},18} = 5, 10, 15, 20,$  and  $25$ . The red lines correspond to  $R_{^{13},18} = 17.0$  and  $14.5$ , which are the values for the Orion Bar and DLSF, respectively. The white lines correspond to  $R_{^{13},18} = 12.15, 11.7, 11.4,$  and  $10.1$ , which are the values for the OMC-1, OMC-2/3, OMC-4, and the bending structure, respectively.

remains valid that the  $X_{^{13}\text{CO}}/X_{\text{C}^{18}\text{O}}$  values are higher than solar throughout Orion A, and larger in the PDRs than in the diffuse medium.

*Acknowledgements.* We acknowledge the anonymous referee for providing helpful suggestions to improve this paper. The 45-m radio telescope is operated by Nobeyama Radio Observatory, a branch of National Astronomical Observatory of Japan. This work was supported by JSPS KAKENHI Grant Number 90610551. Part of this work was supported by the ANR-11-BS56-010 project “STARFICH”.

## References

- Arzoumanian, D., André, P., Didelon, P., et al. 2011, *A&A*, 529, L6  
 Bally, J., Langer, W. D., Stark, A. A., & Wilson, R. W. 1987, *ApJ*, 312, L45  
 Berné, O., Marcelino, N., & Cernicharo, J. 2010, *Nature*, 466, 947  
 Buckle, J. V., Davis, C. J., Francesco, J. D., et al. 2012, *MNRAS*, 422, 521  
 Castets, A., Duvert, G., Dutrey, A., et al. 1990, *A&A*, 234, 469  
 Chini, R., Reipurth, B., Ward-Thompson, D., et al. 1997, *ApJ*, 474, L135  
 Davis, C. J., Froebrich, D., Stanke, T., et al. 2009, *A&A*, 496, 153  
 Dutrey, A., Duvert, G., Castets, A., et al. 1993, *A&A*, 270, 468  
 Elias, J. H. 1978, *ApJ*, 224, 857  
 Emerson, D. T., & Graeve, R. 1988, *A&A*, 190, 353  
 Frerking, M. A., Langer, W. D., & Wilson, R. W. 1982, *ApJ*, 262, 590  
 Glassgold, A. E., Huggins, P. J., & Langer, W. D. 1985, *ApJ*, 290, 615  
 Goudis, C. 1982, *The Orion complex: A case study of interstellar matter* (Dordrecht: D. Reidel Publishing Co), *Astrophys. Space Sci. Lib.*, 90  
 Hirota, T., Ando, K., Bushimata, T., et al. 2008, *PASJ*, 60, 961  
 Hollenbach, D. J., & Tielens, A. G. G. M. 1997, *ARA&A*, 35, 179  
 Hollenbach, D. J., & Tielens, A. G. G. M. 1999, *Rev. Modern Phys.*, 71, 173  
 Ikeda, N., & Kitamura, Y. 2009, *ApJ*, 705, L95  
 Ikeda, N., Sunada, K., & Kitamura, Y. 2007, *ApJ*, 665, 1194  
 Johnstone, D., & Bally, J. 1999, *ApJ*, 510, L49  
 Kawamura, A., Onishi, T., Yonekura, Y., et al. 1998, *ApJS*, 117, 387  
 Kim, S.-J., Kim, H.-D., Lee, Y., et al. 2006, *ApJS*, 162, 161  
 Lada, C. J., Lada, E. A., Clemens, D. P., & Bally, J. 1994, *ApJ*, 429, 694  
 Langer, W. D., Graedel, T. E., Frerking, M. A., & Armentrout, P. B. 1984, *ApJ*, 277, 581  
 Lee, K., Looney, L. W., Schnee, S., & Li, Z.-Y. 2013, *ApJ*, 772, 100  
 Liszt, H. S. 2007, *A&A*, 476, 291  
 Menten, K. M., Reid, M. J., Forbrich, J., & Brunthaler, A. 2007, *A&A*, 474, 515  
 Nagahama, T., Mizuno, A., Ogawa, H., & Fukui, Y. 1998, *AJ*, 116, 336  
 Nakamura, F., Miura, T., Kitamura, Y., et al. 2012, *ApJ*, 746, 25  
 Nummelin, A., Dickens, J. E., Bergman, P., et al. 1998, *A&A*, 337, 275  
 Onishi, T., Mizuno, A., Kawamura, A., Ogawa, H., & Fukui, Y. 1996, *ApJ*, 465, 815  
 Palmeirim, P., André, P., Kirk, J., et al. 2013, *A&A*, 550, A38  
 Rodríguez-Franco, A., Wilson, T. L., Martín-Pintado, J., & Fuente, A. 2001, *ApJ*, 559, 985  
 Röllig, M., & Ossenkopf, V. 2013, *A&A*, 550, A56  
 Sandstrom, K. M., Peek, J. E. G., Bower, G. C., Bolatto, A. D., & Plambeck, R. L. 2007, *ApJ*, 667, 1161  
 Sawada, T., Ikeda, N., Sunada, K., et al. 2008, *PASJ*, 60, 445  
 Schwab, F. R. 1984, in *Indirect Imaging. Measurement and Processing for Indirect Imaging*, ed. J. A. Roberts (Cambridge University Press), 333  
 Shimajiri, Y., Takahashi, S., Takakuwa, S., Saito, M., & Kawabe, R. 2008, *ApJ*, 683, 255  
 Shimajiri, Y., Takahashi, S., Takakuwa, S., Saito, M., & Kawabe, R. 2009, *PASJ*, 61, 1055  
 Shimajiri, Y., Kawabe, R., Takakuwa, S., et al. 2011, *PASJ*, 63, 105  
 Shimajiri, Y., Sakai, T., Tsukagoshi, T., et al. 2013, *ApJ*, 774, L20  
 Sorai, K., Sunada, K., Okumura, S. K., et al. 2000, in *Radio Telescopes*, ed. H. R. Butcher, *SPIE Conf. Ser.*, 4015, 86  
 Sunada, K., Yamaguchi, C., Nakai, N., et al. 2000, in *Radio Telescopes*, ed. H. R. Butcher, *SPIE Conf. Ser.*, 4015, 237  
 Tatematsu, K., Umemoto, T., Kameya, O., et al. 1993, *ApJ*, 404, 643  
 Tatematsu, K., Jaffe, D. T., Plume, R., Evans, II, N. J., & Keene, J. 1999, *ApJ*, 526, 295  
 Takahashi, S., Saito, M., Ohashi, N., et al. 2008, *ApJ*, 688, 344  
 Takahashi, S., Ho, P. T. P., Teixeira, P. S., Zapata, L. A., & Su, Y.-N. 2013, *ApJ*, 763, 57  
 Wang, M., Chin, Y.-N., Henkel, C., Whiteoak, J. B., & Cunningham, M. 2009, *ApJ*, 690, 580  
 Warin, S., Benayoun, J. J., & Viala, Y. P. 1996, *A&A*, 308, 535  
 Wilson, T. L. 1999, *Rep. Prog. Phys.*, 62, 143  
 Wilson, T. L., & Matteucci, F. 1992, *A&ARv*, 4, 1  
 Yoshida, A., Kitamura, Y., Shimajiri, Y., & Kawabe, R. 2010, *ApJ*, 718, 1019  
 Yurimoto, H., & Kuramoto, K. 2004, *Science*, 305, 1763